Calculated X-Ray Backlighting Images of Mixed Imploded Targets

Shell-core mixing, which can occur during the deceleration phase of a laser-driven implosion, is believed to be the major limitation on target performance. This mixing is brought about by a hydrodynamic instability during the deceleration phase, which is seeded by instability generated during the acceleration phase due to laser and target nonuniformities.[1] The image of the x-ray emission from the shell (enhanced by high-Z doping) was used in recent experiments to diagnose this effect.[2] Because of the limb effect, this emission appears in the image in the form of a ring; mixing causes this emission ring to move toward smaller radii. However, the difference in the image characteristics between mixed targets and unmixed targets, which compress to a smaller radius, is subtle: in the former case, the outward drop in intensity is slower. Thus, a smaller compression and mixing tend to cancel each other's effect on the position of the ring in the image.

We show here that when backlighting imaging is used in the experiment, that uncertainty can be largely removed. An important ingredient of such imaging is the ability to record simultaneously the backlighting image as well as the image due to the target self-emission. We showed earlier[3,4] that to achieve this requirement, the image has to be monochromatized by a diffracting crystal because self-emission from predicted OMEGA Upgrade targets was shown to completely overwhelm the intensity of any backlighting radiation. However, if most of the backlighter radiation is comprised in a single spectral line to which the monochromator is tuned, the two image components can be made to have comparable intensities.
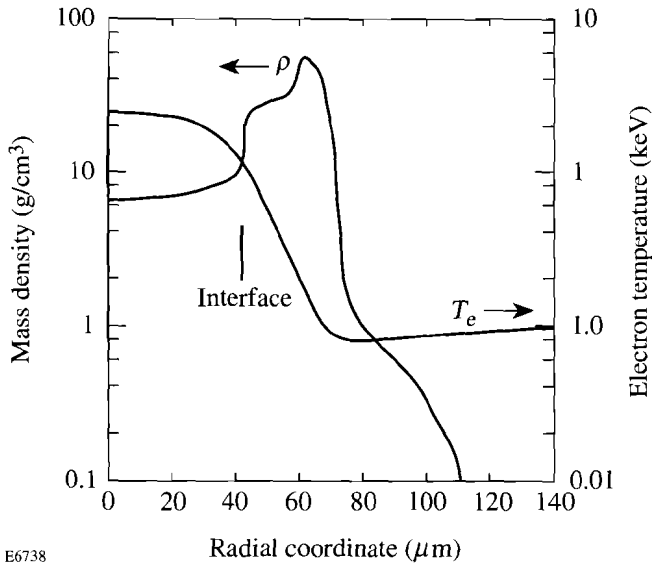
An absorption ring appears in the image, outside the ring due to target self-emission, when the proper backlighter conditions are chosen. The results of this work show that, whereas the emission ring indeed moves to smaller radii when mixing is introduced, the backlighting absorption ring is virtually unaffected. Thus, the relative position of the two rings constitutes a mixing signature. In other words, the absorption ring delineates the colder part of the shell and is a true signature of the compression, whereas the emission ring reflects the shell material motion due to mixing.

We calculate here the combined backlighting and self-emission image of a particular simulated target implosion on the OMEGA Upgrade laser. For this test case, *LILAC* results were used for the expected temperature and density profiles of the unmixed target. A post-processor code was developed[4] to calculate the transport of backlight radiation through the target, as well as the self-emission of the target itself (and its transport). A simplified procedure is used to simulate the mixing, and the radiation transport equation is then solved for the unmixed as well as the mixed targets. The total calculated image has two components that are measured simultaneously: the one due to the backlighting, and the other due to target self-emission. The former is calculated assuming a certain incident flux level, based on experiments; the latter is directly calculated from the *LILAC* profiles, using the radiation transport code developed here.

The target is a polymer shell of 940-μm diameter and 30-μm thickness, filled with 80 atm DT gas, and imploded by a trapezoidal pulse. The pulse rises linearly over a 0.1-ns period to 13.5 TW, then remains constant for 2.2 ns, before dropping linearly over a 0.1-ns period. Figure 59.16 shows the density and electron-temperature profiles predicted for this target at peak compression. The shell material has been compressed to a mean radius of ~50 μm and thickness of ~30 μm, with a density in the range of ~10 to 50 g/cm^3, corresponding to a $\rho\Delta r$ value of ~90 mg/cm^2. The electron temperature in the shell ranges from ~80 to ~800 eV. Most of the backlight radiation absorption will occur within the colder, outer part of this compressed shell.

Modeling of Target Mixing

We follow a procedure suggested by Landen *et al.*[2] for choosing the size of the spatial region over which mixing occurs during the deceleration (or burn) phase of the implosion. It is implicitly assumed that the instability during the acceleration phase is not severe enough to disrupt the shell, but it only seeds the instability due to the deceleration. Figure 59.17 describes the procedure. The $R_i(t)$ curve represents the motion of the fuel-shell interface. The free-fall line $R_{ff}(t)$ is a constant-velocity trajectory tangent to the $R_i(t)$ curve
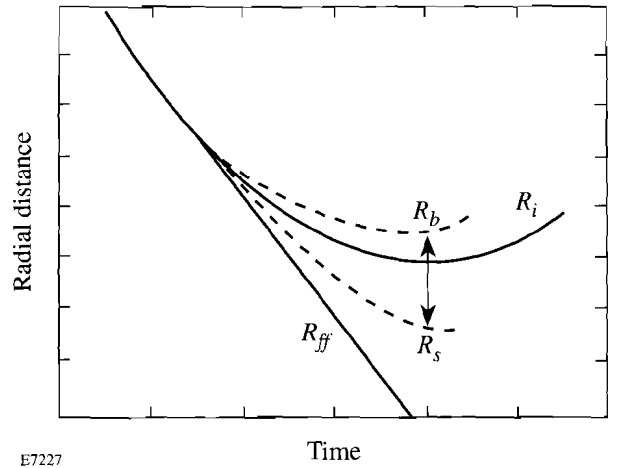
E6738

The density and electron-temperature profiles predicted by the *LILAC* code at peak compression for the case studied in this article.

E7227

Figure 59.17

Schematic description of trajectories defining the mixed region [according to Eq. (1)]. R_i is the shell-fuel interface, R_{ff} the free-fall line, R_s the edge of the spikes region, and R_b the edge of the bubbles region. The mixed region extends from R_s to R_b.

at a time when the implosion velocity is maximal. A mixed region of $F\%$ means that the deepest penetration of shell material into the fuel region spans $F\%$ of the distance between the $R_i(t)$ curve and the free-fall line. Comparison with implosion experiments[2] on NOVA yielded a value of $F \sim 20\%$; we show here results of calculations using this value and higher degrees of mixing. Simulations of Rayleigh-Taylor unstable implosions[5] show that in the nonlinear regime of the instability the shell (the heavier fluid) penetrates into the fuel (the lighter fluid) in the form of spikes. In between the spikes the fuel penetrates into the shell region in the form of bubbles whose penetration span is typically half that of the penetration of the spikes. We refer to the region comprised between $R_s(t)$ and $R_b(t)$ as the mixed region. In Fig. 59.17 the curves delineating the extreme positions of the spikes $R_s(t)$ and the bubbles $R_b(t)$ are shown schematically. Theory shows that for Atwood number 1 the amplitude of the spikes (measured from the unperturbed interface position) is twice that of the bubbles.[6] More specifically, for $F = 0.2$ the trajectories $R_s(t)$ and $R_b(t)$ will be given by

$$R_i(t) - R_s(t) = 0.2\left[R_i(t) - R_{ff}(t)\right],$$

$$R_b(t) - R_i(t) = 0.1\left[R_i(t) - R_{ff}(t)\right]. \tag{1}$$

The $R_i(t)$ curve for the test case analyzed here was plotted, and the parameters of the mixed region [$R_s(t)$ and $R_b(t)$] were determined as a function of time. At peak compression, the interface position with no mixing was $R_i = 42.7$ μm, whereas the parameters of the mixed region for two particular values of F were

for $F = 0.2$: $\quad R_s = 34.5\,\mu m, \quad\quad R_b = 45.5\,\mu m$

$$\tag{2}$$

for $F = 0.4$: $\quad R_s = 26.6\,\mu m, \quad\quad R_b = 50.0\,\mu m.$

Once the mixed region boundaries are thus determined, the procedure for the actual mixing must be determined. The manner in which the material is assumed mixed within the mixed region is somewhat arbitrary. We choose a simple prescription where the mixing is not uniform but rather decays with distance. The choice is made separately for the density of carbon ions (hence the density of shell material) and for the density of fuel ions. Using these choices, other parameters are calculated: the fraction of carbon ions out of the total ion density, the average charge $\langle z \rangle$, the total electron density, and the temperature. Figure 59.18 shows the mixing choices for the shell material and fuel (and some resulting distributions) for the test case, at peak compression (2.9 ns). Figure 59.18(a) shows the density N_C of carbon ions (atomic absorption calculations are done for C and H separately). The unmixed density curve is taken from *LILAC* runs, such as in Fig. 59.16. The

mixed curve for N_C is assumed to start from zero at R_s and to extend linearly with distance up to R_b. The slope of the curve is determined by the requirement that the mixing conserves mass (or the number of ions). As seen, this results in a jump at the $r = R_b$ position. This is not surprising if we note that the mixed profiles, such as the $N_C(R)$ curve in Fig. 59.18(a), represent lateral averages over the varying spike-bubble structure of the unstable region. The smearing, implicit in our assumption that the curves depend only on r, results in a sharp drop in laterally averaged density when crossing from the unmixed to the bubbles region.

Figure 59.18(b) shows the choice for the mixed profile of the fuel, N_F, using a slightly different prescription than that applied to the shell; N_F stands for the total density of D and T ions. The mixed curve is assumed to start from 0 at $r = R_b$ and to extend linearly inward up to the point where it meets the

unmixed curve. Again, the slope of the curve is determined by the requirement that the mixing conserves mass. Because of the spike in the unmixed fuel profile near the interface, extending the linear profile all the way to $r = R_s$ would cause a transfer of fuel material from the spike inward, not only outward. Because of the choice made here, part of the fuel in the mixed region remains unaffected by the mixing (the fuel comprised between $r = 26.6$ and $r = 36.0$ μm).

To check how reasonable the resulting profiles are, we calculate the carbon fraction, defined as

$$f_C = N_C/(N_F + N_C + N_H). \qquad (3)$$

Figure 59.18(c) shows that f_C is reasonably smooth and indeed reaches the correct boundary conditions: 0.5 at $r = R_b$
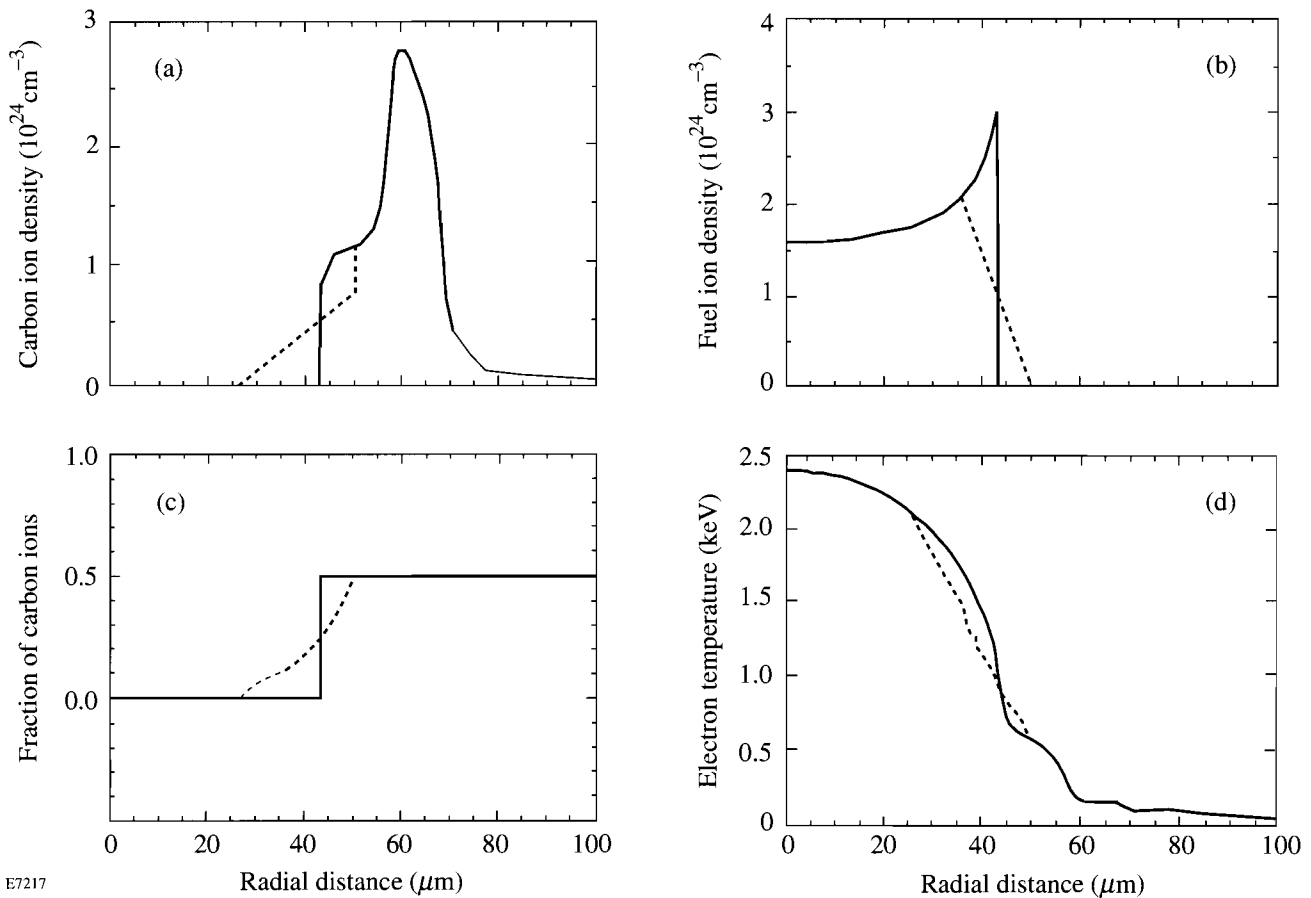

Figure 59.18
Radial profiles in the unmixed (——) and mixed (- - -) target, for $F = 0.4$ mixing: (a) the chosen distribution of carbon ion density (half the CH ion density), (b) the chosen distribution of fuel ions (half of which is D, half T), (c) the calculated distribution of the fraction of carbon ions among all hydrogenic ions (H, D, and T), and (d) the calculated distribution of the electron temperature. The shell-fuel interface position with no mixing is at 42.7 μm.

and 0 at $r = R_s$. A similar behavior is seen by the profile of the average charge.

We next calculate the effect of mixing on the temperature and electron density. We assume that the radial ordering of any two shell elements that moved into the fuel is the same as they had before moving, and likewise for fuel elements. We further assume that both CH or fuel material carry their own temperature as they move to new locations, where their temperature is then averaged with the local temperature (of material that has not moved). For example, the innermost shell cell in the unmixed target is assumed to map onto a region in the mixed target extending from $r = R_s$ outward, until the total mass in that cell is exhausted; a similar transfer holds for all consecutive shell cells within the mixed region. For the fuel, the outermost cell in the unmixed target maps in the mixed target onto the region extending from $r = R_b$ inward, etc. Once the temperatures of the fuel and shell elements in each zone are determined, the final temperature is given by the average of the two, weighted by the corresponding densities. The same applies to both the electron and ion temperatures. The unmixed and mixed electron temperature profiles at peak compression are shown in Fig. 59.18(d). Obviously, colder shell material lowered the temperature of the fuel region it migrated to, whereas hotter fuel material raised the temperature of the shell region it migrated to. Updating the electron density is similar to updating the temperature. The average charge $\langle z \rangle$ in each unmixed shell zone maps onto the corresponding mixed zones as before; the final electron density is given by $N_e = 2\langle z \rangle N_C + N_F$.

The modeling of target mixing, where a given shell layer is doped with a high-Z dopant, follows the same procedure as outlined above. Namely, the dopant material follows the CH element in which it was embedded initially, and the percentage of doping remains the same. The modeling used here does not include self-consistent feedback, i.e., the effect of mixing in one time step upon the hydrodynamics and radiation physics in subsequent steps. The limitations resulting from this simplification will be further discussed below.

Backlighting and Self-Emission Images of Unmixed Targets

Next we study the ability to diagnose mixing through its effect on target images due to both self-emission and backlighting. The problem of backlighting, including that of doped targets, has been studied previously.[4] In Fig. 59.19 we show an image of a doped but unmixed target, at $\lambda = 1.48$ Å (the helium-like resonance line of Cu^{+27}), and then show how it

changes when mixing is introduced. The total image is due to both self-emission and backlighting (for distances $\gtrsim 45$ μm the self-emission is negligible, and the total image is due to backlighting). The two vertical bars mark the boundaries of the doped region (the left bar also marks the interface). The curves in Fig. 59.19 assume diffraction off a crystal of 4-eV bandwidth (rocking-curve width). As seen, the two image components have comparable intensity, which will be shown below to be essential for the diagnostic method. Without monochromatization, the self-emission will overwhelm the backlighting image and render the method impractical. Thus, if instead of using a monochromator we were to use a filter, the intensity of the monochromatic backlighting radiation (consisting mostly of a single spectral line) will remain about the same. However, the intensity of the continuous self-emission will greatly increase because the filter bandpass will be ~ 1 keV, as compared to the crystal bandpass of ~ 4 eV. The spike at $r = 43$ μm is emitted by the shell's inner surface. It exists because the CH shell has a higher Z than the fuel, but only the inner surface of the shell is hot enough to emit at short wavelengths. With no mixing the spike is too narrow to be easily measurable.
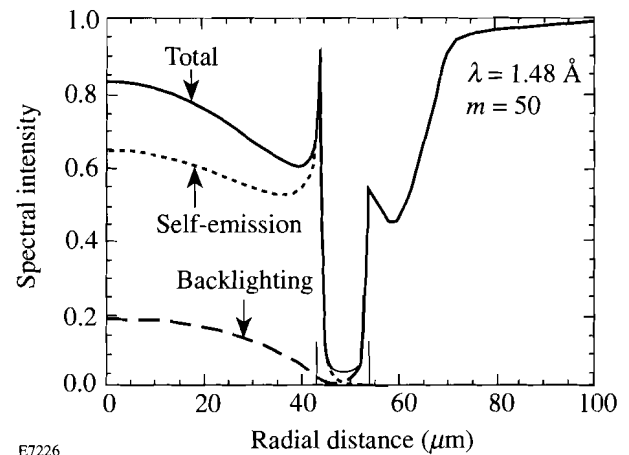

E7226

Figure 59.19
The total image due to self-emission and backlighting at $E = 8.39$ keV ($\lambda = 1.48$ Å), with no mixing. The curves are normalized to a spectral intensity of 1.4×10^{20} keV/$(\text{keV ns cm}^2 \, \Omega)$, the assumed backlighter x-ray flux at this wavelength. For distances $\gtrsim 45$ μm the self-emission is negligible, and the total image is due to backlighting. The two vertical bars mark the boundaries of the doped region (the left bar is also the interface).

The curves in Fig. 59.19 are normalized to a spectral intensity of 1.4×10^{20} keV/$(\text{keV ns cm}^2 \, \Omega)$, the assumed backlighter x-ray flux at this wavelength. This spectral flux level is based on x-ray yield experiments[7] using the helium-like resonance line of Cu^{+27} ($\lambda = 1.48$ Å). The image in

Fig. 59.19 is of a doped target, where the inner 2.4 μm have been doped with a high-Z dopant. The motivation for doping is to create a narrower region of absorption so that the delineation of the dense, cold part of the shell be done with greater definition. The initial thickness of the doped layer was chosen so that its width at peak compression (with no mixing) will be resolvable by the imaging instrument. In Fig. 59.19, the width of the absorption ring due to the high-Z dopant (around $r \sim$ 50 μm) is about $\Delta r = 8.6$ μm, well within the resolving capability of our x-ray microscopes. Additionally, the outer absorption ring (around $r \sim$58 μm) is due to absorption in the undoped CH shell. It corresponds to the maximum in the shell density (see Fig. 59.16). On moving to smaller radii, the absorption in the CH decreases partly because of a decrease in the shell density, but mainly because of a rise in the temperature. Figure 59.19 shows clearly the benefit of doping the target: it reduces significantly the width of the absorption region. It also explains the choice of backlighting wavelength: for the absorption in the doped part of the shell to be dominant, the wavelength must be short enough so that the CH absorption is small (see Fig. 59.22 for an image of an undoped target at a longer backlighting wavelength).

Doping was modeled here in a simplified way—by multiplying the total absorption coefficient of the undoped target by a factor m ($m = 50$ in Fig. 59.19). The total calculated absorption coefficient includes bound-free and free-free absorptions.[4] Irrespective of the detailed atomic physics of a high-Z dopant, its final effect is to increase the absorption coefficient and, through it, the local emission (which was related to the absorption coefficient through the Kirchhoff's law). To simulate doping we therefore multiply the absorption coefficient (and thereby also the emission coefficient) by a number m. The only information that is indeterminate here is the quantity of a given type of dopant corresponding to each m.

Calculations with different thicknesses of the doped layer show that the initial thickness of 2.4 μm for the test shot considered here is about optimal. For thinner doped layers the resulting absorption dip may be difficult to resolve, at least in the absence of severe mixing. For thicker doped layers, the outer part of the doped layer is at a low temperature during peak compression. Thus, the temperature where the doped layer absorbs most in Fig. 59.19 is around 400 eV, whereas a thicker doped layer will extend the absorption to regions of temperatures down to ~100 eV, where the absorption is much higher. Such increased absorption causes severe attenuation of the self-emission, particularly from the region near the interface, thus obliterating the sharp rise in intensity seen at $r \sim$45 μm.

In order to estimate the amount of doping corresponding to a given m we must apply a non-LTE collisional-radiative model to a given high-Z dopant. If the doping is not negligibly small, we must also recompute the hydrodynamic evolution of the doped target. Instead, we make a rough estimate of the doping level corresponding to $m = 50$ if the chosen dopant is chlorine. It has been shown[4] that most of the shell absorption in carbon is due to the bound-free (photo-ionization) process; this is certainly true for any higher-Z dopant. For most of the shell the chlorine ions will be ionized to the helium-like state so that their average Z will be ~15. Since the bound-free absorption coefficient depends on Z like Z^4 (for a given ion density), we estimate that to achieve $m = 50$, the density of chlorine ions should be about the same as that of carbon ions. Higher-Z doping elements will require a lower doping level for the same value of m. Also, a lower value of m can be acceptable if a smaller absorption dip can be tolerated.

Backlighting and Self-Emission Images of Mixed Targets

We now apply the mixing procedure as described earlier to the test target at peak compression and then apply the radiation transport post-processor to calculate the backlighting and self-emission images.

Figures 59.20 and 59.21 show the combined image with and without mixing. The degree of mixing in Fig. 59.20 is $F =$ 0.2; in Fig. 59.21 it is $F = 0.4$. The unmixed image is from Fig. 59.19. As mentioned above, comparison with experiments reported previously agreed with a value of $F = 0.2$. Mixing has two effects on the image: (a) the spike of self-emission greatly broadens spatially and moves toward the target center, and (b) its intensity increases dramatically. Both of these effects are caused by CH material moving into higher-temperature regions within the fuel. For $F = 0.2$ the spike moves from $r =$ 44 μm to $r = 37$ μm, and its peak intensity increases by about a factor of 12.5. For $F = 0.4$ the spike moves from $r = 44$ μm to $r = 32$ μm, and its peak intensity increases by about a factor of 40. The spike in these two cases broadens to a width of about 5 μm and 9 μm, respectively. The predicted increase in intensity is easily measurable, but the shifts and broadenings are still within the capabilities of the OMEGA Upgrade diagnostics.

The most striking feature in Figs. 59.20 and 59.21 is the fact that the absorption dip is hardly affected by the introduction of mixing. Thus, the measured separation between the emission peak and absorption dip (both of which appear as rings in the two-dimensional image) is a convenient signature of the degree of mixing. As stressed above, the calculations performed here do not account for the feedback effect of the mixing on the
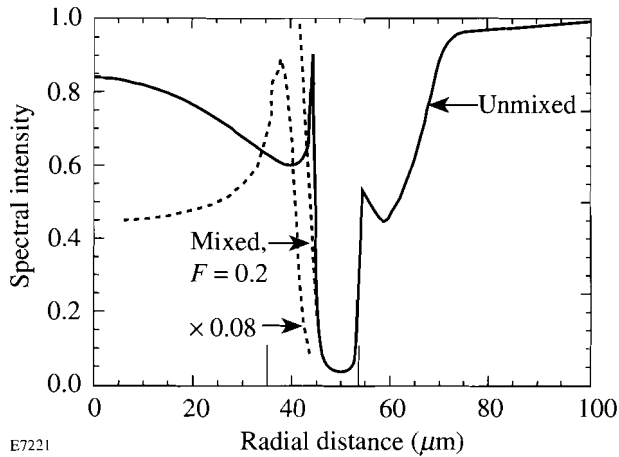
E7221

Figure 59.20
The total image at λ = 1.48 Å due to self-emission and backlighting for unmixed and mixed targets (with a degree of mixing F = 0.2). The unmixed image is from Fig. 59.19. The curves are normalized to a spectral intensity of 1.4×10^{20} keV/$\left(\text{keV ns cm}^2 \Omega\right)$. The two vertical bars mark the boundaries of the doped region (in the mixed target). The shell-fuel interface position with no mixing is at 42.7 μm.
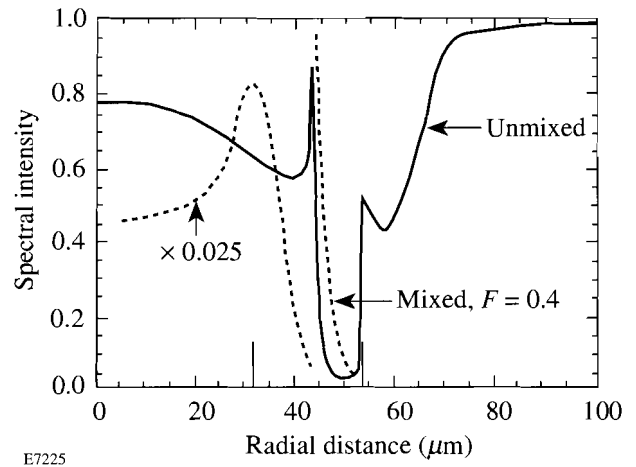

E7225

Figure 59.21
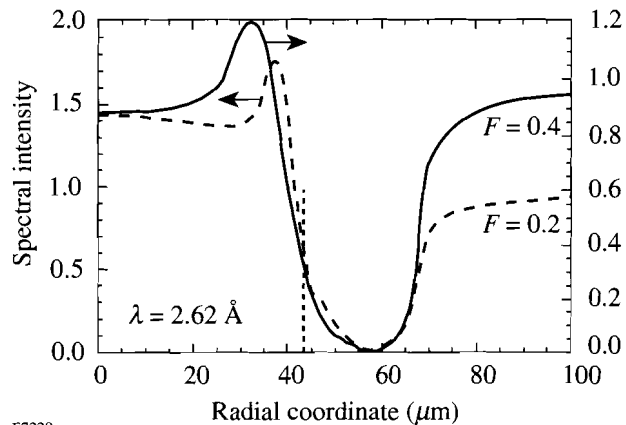The total image at λ = 1.48 Å due to self-emission and backlighting for unmixed and mixed targets (with a degree of mixing F = 0.4). The unmixed image is from Fig. 59.19. The curves are normalized to a spectral intensity of 1.4×10^{20} keV/$\left(\text{keV ns cm}^2 \Omega\right)$. The two vertical bars mark the boundaries of the doped region (in the mixed target). The shell-fuel interface position with no mixing is at 42.7 μm.

hydrodynamic and thermodynamic target evolution. The main effect of such a feedback is expected to be the lowering of the temperature in the fuel region due to radiation cooling by the high-Z contaminant (which includes CH material and any dopant assumed in the initial target). This cooling will reduce the intensity of the emission peak. However, the general statement will still be valid, that the absorption dip is a signature of the position of the compressed shell, whereas the emission peak is a measure of the penetration of shell material into the fuel. *Thus, a very useful comparison of experiment and theoretical predictions can be obtained if the imaging includes a backlighting component in addition to the self-emission image.*

Finally, we discuss the effect of mixing on the backlighting image of undoped targets. Since, as we have seen earlier, the absorption of 1.48-Å radiation in the test target with no doping is very small, we increase the backlighting wavelength to 2.62 Å (the wavelength of the helium-like resonance line of Ti^{+20}). Figure 59.22 shows the combined backlighting and self-emission images for two degrees of mixing, F = 0.2 and F = 0.4. The spectral flux is normalized to that expected[7,8] from a titanium backlighter: 7.0×10^{20} keV/$\left(\text{keV ns cm}^2 \Omega\right)$. Undoped targets give rise to a broader, less-well-defined absorption peak. However, the target fabrication is simpler, and, due to the longer wavelength, the intensity is higher. Comparing Fig. 59.22 to Figs. 59.20 and 59.21 shows that the

position of the emission peaks for a given F value is almost the same for the two different wavelengths. However, the increase in intensity is not as dramatic as with the shorter wavelength. As recalled, the increase in intensity of the self-emission is due to shell material moving into higher temperature regions in the core. The intensity is governed by factors of the type $\exp\left[-(E/kT)\right]$, where E is the photon energy. Thus, when E is higher (as is the case in Figs. 59.20 and 59.21), the intensity increases faster with increasing temperature.

The fact that the peak position is about the same for the two wavelengths (for the same level of mixing) supports the contention that a fully consistent calculation of the mixed target evolution should result in a similar shift of the emission peak. Radiation cooling will certainly reduce the emission peak intensity, but the peak position will depend primarily on the length of mixing and less on the temperature. The peak appears roughly at the position of maximum penetration of the shell material into the fuel because the temperature there is maximal over the penetration depth. We have calculated images such as in Figs. 59.20–59.22 for increasing F values, up to the maximum of F ~0.7; at that value of F the free-fall line (see Fig. 59.17) reaches the target center by the time of peak compression. In all these cases the absorption dip position and depth remain about the same. This means that the observation of significant deviations from the predicted characteristics of the absorption ring is evidence of more severe instability, such

E7229

Figure 59.22

The combined backlighting and self-emission image of the test target with no doping, at $\lambda = 2.62$ Å, and two degrees of mixing: $F = 0.2$ and $F = 0.4$. The curves are normalized to a spectral intensity of 7.0×10^{20} keV$/(\text{keV ns cm}^2 \Omega)$. The vertical dashed bar marks the position the shell-fuel interface would have without mixing.

as shell disruption on the way in, due to initial nonuniformity. Finally, the measured absorption depth (i.e., the attenuation of backlighting radiation) can be used for comparison with predictions. This attenuation depends both on the shell temperature and the shell $\rho\Delta r$. The position of the absorption ring can be used to deduce the fuel compression and the presence of low-order nonuniformity of the compressed core.

REFERENCES

1. J. D. Lindl, R. L. McCrory, and E. M. Campbell, Phys. Today **45**, 32 (1992).

2. O. L. Landen, W. K. Levedahl, and T. R. Dittrich, Bull. Am. Phys. Soc. **38**, 2083 (1993).

3. B. Yaakobi, F. J. Marshall, Q. Su, and R. Epstein, to appear in the Journal of X-Ray Science and Technology.

4. Laboratory for Laser Energetics LLE Review **58**, NTIS document No. DOE/SF/19460-17, 1994 (unpublished), p. 57.

5. C. P Verdon, R. L. McCrory, R. L. Morse, G. R. Baker, D. I. Meiron, and S. A. Orszak, Phys. Fluids **25**, 1653 (1982).

6. D. L. Youngs, Physica **12D**, 32 (1984); S. W. Haan, Phys. Rev. A **39**, 5812 (1989); N. Freed, D. Ofer, D. Shvarts, and S. A. Orszag, Phys. Fluids A **3**, 912 (1991).

7. B. Yaakobi, P. Bourke, Y. Conturie, J. Delettrez, J. M. Forsyth, R. D. Frankel, L. M. Goldman, R. L. McCrory, W. Seka, J. M. Soures, A. J. Burek, and R. E. Deslattes, Opt. Commun. **38**, 196 (1981).

8. D. L. Matthews *et al.*, J. Appl. Phys. **54**, 4260 (1983).